




Surface precipitation of supersaturated solutes in a ternary Fe–Au–W alloy and its binary counterparts

Y. Fu^{1,2,*} , C. Kwakernaak³, J. C. Brouwer³, W. G. Sloof³, E. Brück¹, S. van der Zwaag^{2,4}, and N. H. van Dijk¹

¹ Fundamental Aspects of Materials and Energy Group, Faculty of Applied Sciences, Delft University of Technology, Mekelweg 15, 2629 JB Delft, The Netherlands

² Novel Aerospace Materials Group, Faculty of Aerospace Engineering, Delft University of Technology, Kluyverweg 1, 2629 HS Delft, The Netherlands

³ Department of Materials Science and Engineering, Delft University of Technology, Mekelweg 2, 2628 CD Delft, The Netherlands

⁴ School of Materials Science and Engineering, Tsinghua University, Beijing 100084, China

Received: 22 July 2020

Accepted: 13 November 2020

Published online:

30 November 2020

© The Author(s) 2020

ABSTRACT

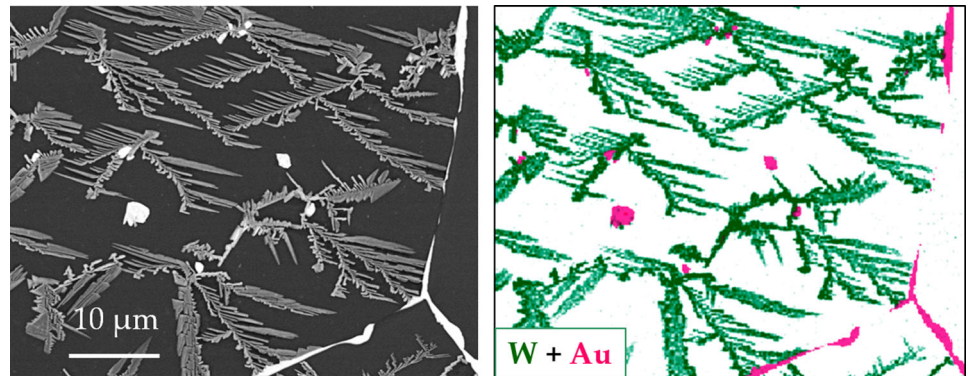
The precipitation of supersaturated solutes at free surfaces in ternary Fe–3Au–4W and binary Fe–3Au and Fe–4W alloys (composition in weight percentage) for different ageing times was investigated at a temperature of 700 °C. The time evolution of the surface precipitation is compared among the three alloys to investigate the interplay between the Au and W solutes in the ternary system. The Au-rich grain-interior surface precipitates show a similar size and kinetics in the Fe–Au–W and Fe–Au alloys, while the W-rich grain-interior surface precipitates show a smaller size and a higher number density in the Fe–Au–W alloy compared to the Fe–W alloy. The kinetics of the precipitation on the external free surface for the ternary Fe–Au–W alloy is compared to the previously studied precipitation on the internal surfaces of the grain-boundary cavities during creep loading of the same alloy.

Handling Editor: P. Nash.

Address correspondence to E-mail: Y.Fu-1@tudelft.nl

<https://doi.org/10.1007/s10853-020-05571-w>

GRAPHICAL ABSTRACT



Introduction

Metals in service degrade due to processes like creep, fatigue, wear, corrosion, and radiation damage. Traditionally, efforts have been made to stabilize the material composition and microstructure so that the occurrence of damage is postponed as long as possible, which corresponds to a damage prevention strategy [1]. Since the initiation of the damage is assumed to be inevitable, the concept of self-healing is proposed as an alternative strategy, in which case the occurrence of damage triggers mobile healing agents to move towards the defect and heal the defect site [2, 3]. In the self-healing approach, the propagation of damage is interrupted.

The self-healing concept has been applied to improve the creep resistance [4–7], fatigue resistance [8, 9] and the radiation damage resistance [10] of various metallic systems. The combined addition of boron and nitrogen into austenitic stainless steels (with an *fcc* lattice structure) is effective in reducing the cavity growth rate, as well as increasing the creep rupture strength [4, 11]. The self-healing behaviour was studied in underaged Al alloys subjected to creep [5, 8] and fatigue [8] conditions. The healing solutes (usually Cu atoms) migrate to the defects and form precipitates via bulk diffusion or pipe diffusion along dislocations. The improvement in creep and fatigue performance is achieved by dynamic precipitation, the subsequent reduction in the dislocation mobility and/or the closure of the incipient cracks. It

has been demonstrated that Au atoms dissolved in *bcc* iron can actively heal early-stage radiation damage by solute segregation [10]. In a systematic study on ferritic steels (with a *bcc* lattice structure), a series of binary and ternary alloys [6, 7, 12–17], including Fe–Cu, Fe–Au, Fe–Mo, Fe–W and Fe–Au–W, were investigated to reveal the mechanism of self-healing during creep. The composition of these alloys was selected such that at the operating temperatures the solute is in a supersaturated state by approximately 1 at.%. The supersaturated solute atoms are expected to segregate on the surfaces of the creep-induced grain-boundary cavities and fill them progressively. As a result, the coalescence of neighbouring creep cavities can be prevented or delayed.

One of the challenges in studying the healing of the creep-induced defects lies in the observation of both the creep cavities and the precipitation inside these cavities at different stages of the creep life. In previous studies [7, 16], characterisation techniques, such as scanning electron microscopy (SEM), transmission electron microscopy (TEM) and atom probe tomography (APT), provided extensive information on the microstructure including the composition of the precipitates, the orientation relation between the precipitation and the matrix and the local compositional distribution. Recently, synchrotron X-ray nanotomography was utilized on the Fe–Au and Fe–W systems [12, 13], and 3D structures of the cavities and the healing precipitates were reconstructed with a voxel size down to 25 nm. However, these techniques

are either limited to 2D information (SEM and TEM) or to small 3D regions with a nanometre length scale (APT). The synchrotron X-ray nano-tomography can probe a wider range of length scales in 3D, but can only provide limited access due to the high demand. Sun and co-workers [18] provided a complimentary solution by linking the precipitation on the free creep-cavity surface during creep to the precipitation behaviour on an external surface during ageing. In contrast to a self-healing system during creep loading, where the precipitation is formed on the internal surface of a cavity, in a surface precipitation experiment [19], the solute diffuses towards the external free surface of the sample and forms surface precipitates there. These precipitates at an external surface are much easier to observe than those at internal surfaces. By comparing the growth kinetics of the precipitates formed on the external surface (from surface precipitation experiments) and on the internal surfaces (from self-healing creep experiments), it was demonstrated that the underlying physics for precipitation on the external surface and on internal surfaces is the same [18].

In the present study, the precipitation of supersaturated solutes in *bcc* iron at free surfaces for ternary Fe–3Au–4W and related binary Fe–3Au and Fe–4W alloys (all in weight percentage) is explored. The time evolution of the Au-rich and W-rich precipitates is investigated for different ageing times. This study aims to provide a complimentary method to understand and predict the precipitation behaviour and the mass transfer of supersaturated solutes. The results for the ternary Fe–Au–W alloy are compared with the binary Fe–Au and Fe–W alloys to investigate the interplay between the two healing agents in the ternary system. The Au-rich and W-rich precipitates found in the ternary Fe–Au–W system are consistent with the ones observed in the binary Fe–Au and Fe–W systems. The Au-rich precipitates formed at 700 °C show an *fcc* structure with 60 at.% Au and 40 at.% Fe, while the formed W-rich precipitation corresponds to the hexagonal Fe₂W Laves phase.

Experimental

One ternary Fe–3.07Au–3.80W system and two binary systems, Fe–2.87Au and Fe–3.80W (in weight percentage) were selected for the present surface

precipitation study. The Fe-based alloys were produced by Goodfellow®. Small plates with dimensions of about 10 × 10 × 0.5 mm³ were cut from the as-received rolled sheet materials by spark erosion. Subsequently, the samples were sealed separately in evacuated quartz tubes filled with 200 mbar ultra-high purity argon to prevent oxidation during annealing. The annealing (8 h at 868 °C for the Fe–Au–W and Fe–Au alloys and 24 h at 900 °C for the Fe–W alloy) and the subsequent water quenching were performed to dissolve the solute elements into the single-phase ferritic (*bcc*) matrix. The samples were then polished to an OPS level, ultrasonically cleaned extensively, and subsequently placed in an alumina crucible that was mounted into a horizontal quartz tube furnace (Carbolite MTF 12/38/850, UK) with an inner tube diameter of 30 mm. The temperature in the furnace tube was measured with a NiCr/NiAl (type K) thermocouple at the sample location. To avoid oxidation of the samples, a gas mixture of argon and 10 vol.% hydrogen was used to flush the furnace for about 1 h at a flow rate of 1 L/min before the samples were heated. Prior to admitting the gas mixture to the furnaces, each gas, i.e. Ar and H₂ (both with a purity better than 5 N vol.%, Linde, The Netherlands), was filtered to remove any residual hydrocarbons, moisture and oxygen, with Accosorb (< 10 ppb hydrocarbons), Hydrosorb (< 10 ppb H₂O) and Oxysorb (< 5 ppb O₂) filters (Messer Griesheim, Germany), respectively. To further reduce the oxygen level, the argon was passed through an inline quartz tube filter with titanium powder (100 μm, 99.5 wt% purity, TLS Technik GmbH & Co) heated to 800 °C. The flow of each gas was regulated and monitored using mass flow controllers (Bronkhorst, The Netherlands). After flushing the furnace tube, the crucible was heated and kept at 200 °C for 2 h to remove any oxygen and water adsorbed on the surfaces inside the quartz tube. After that, the samples were heated to 700 °C and held isothermally for different times. After the ageing, the samples were cooled in the furnace to room temperature. Scanning electron microscopy (SEM, JEOL JSM 6500F, Japan) coupled with energy-disperse X-ray spectroscopy (EDS) was used to characterize the samples after the heat treatment. In addition, scanning electron microscopy combined with a xenon plasma focused ion beam (Helios G4 PFIB UXe, Thermo Fisher Scientific, USA) was performed to create cross-sections to obtain information on the precipitation underneath

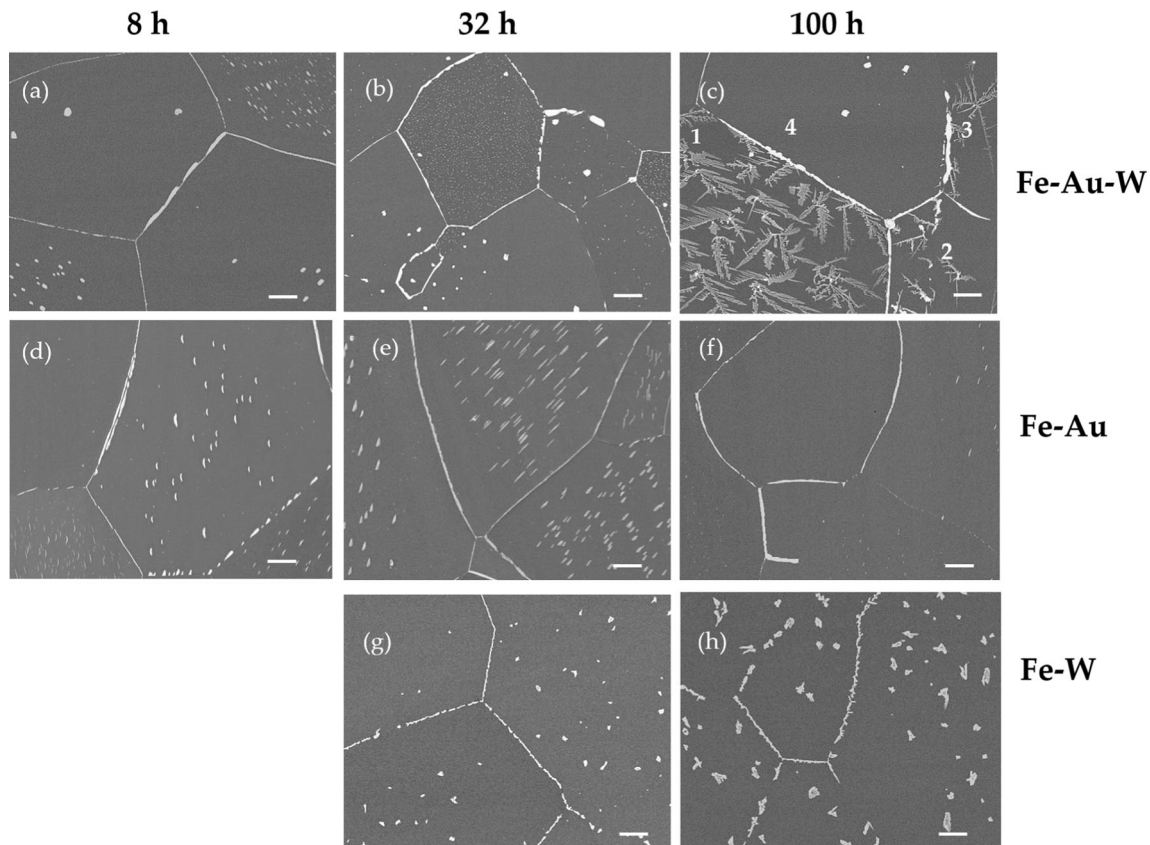


Figure 1 SEM images for the Fe–Au–W, Fe–Au and Fe–W alloys after ageing for different times. **a–c**: Fe–Au–W sample after ageing for 8, 32 and 100 h, respectively; **d–f**: Fe–Au sample after ageing

for 8, 32 and 100 h, respectively; **g, h**: Fe–W sample after ageing for 32 and 100 h, respectively. The scale bars correspond to 10 μm .

the free surface. On small features (cf. Fig. 3g and h), the beam energy employed was 5 keV with an effective analysis volume of about 200 nm across.

Results

The SEM images of the three alloys after ageing for different times are shown in Fig. 1. For all three alloys, the precipitates are found both on and within the perimeter of the grain boundaries. Based on their surface location with respect to the grain boundaries, the precipitates are referred as the grain-boundary (GB) surface precipitates or grain-interior (GI) surface precipitates, respectively. For the precipitates in the Fe–Au alloy, the EDS results show a gold concentration of 40–60 at.%. After ageing for 8 and 32 h (Fig. 1d and e), the GI precipitates vary from grain to grain, in their size, shape and spatial distribution. After 32 h annealing, the GI precipitates are generally larger than their counterparts at 8 h, while after ageing for

100 h, only a limited amount of GI precipitates can be observed for the Fe–Au alloy (Fig. 1f), indicating that most of the Au-rich GI precipitates are collected at the grain boundaries. For the Fe–W samples, the precipitates start to form after 32 h of ageing (Fig. 1g). By EDS, it is observed that the W concentration corresponds to 20–32 at.%. The precipitates show some variation in number density for different grains, but their shapes are similar (Fig. 1g and 1h). From 32 to 100 h, the W-rich precipitates experience an obvious increase in size.

The precipitation in the ternary Fe–Au–W alloy shows more complexity. In the 8 h sample (Fig. 1a), only Au-rich precipitates were found. The GI precipitates in different grains show different shapes and distributions, similar to their counterparts in the Fe–Au sample. On the surface of the 32 h sample, precipitates with different compositions can be observed: the GB precipitation is generally enriched in Au, while the GI precipitates can be (1) enriched in W, (2) enriched in Au and (3) enriched in both W and

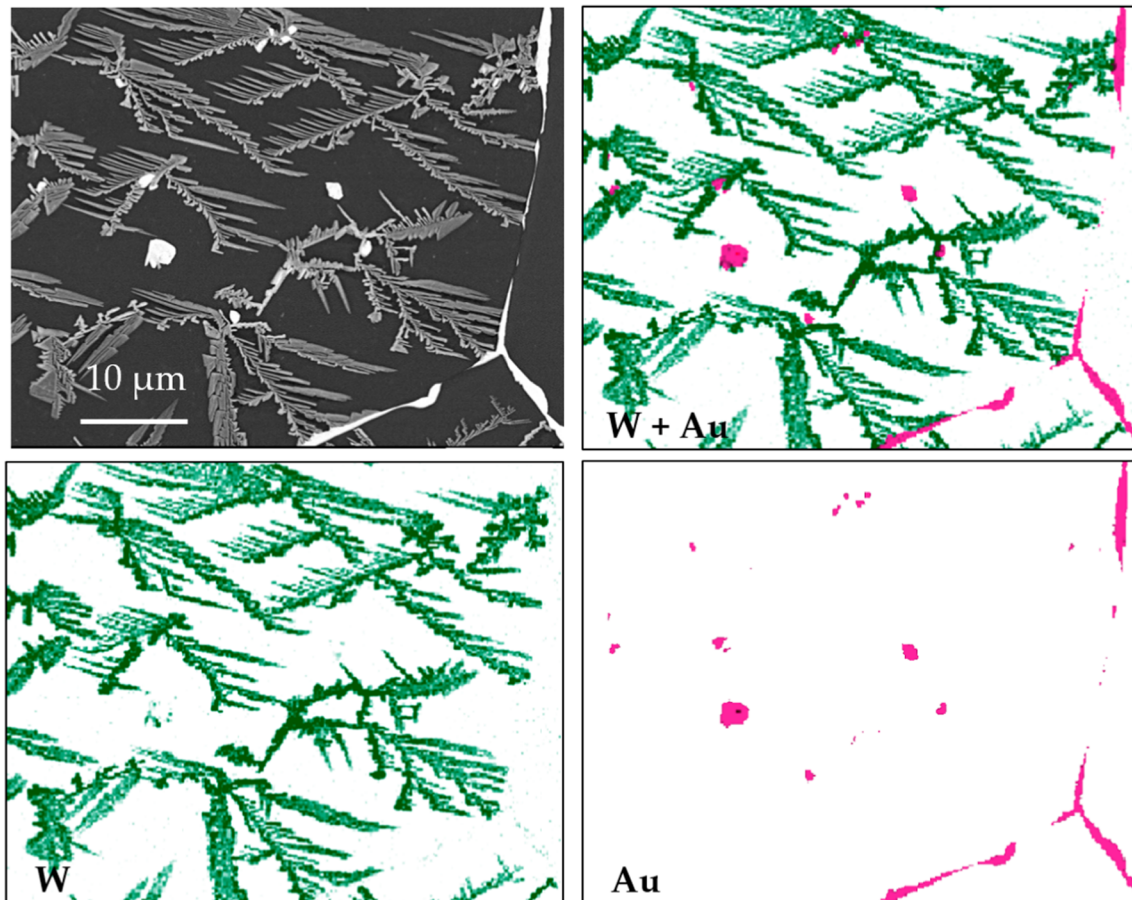


Figure 2 Compositional map of the Fe–Au–W sample after ageing for 100 h.

Au. The W-rich precipitates are the small particles scattered within the perimeter of the grain boundaries. Similar to their counterparts in the Fe–W alloy, the W-rich GI precipitates distribute uniformly in the grains, and usually show irregular shapes with sharp edges. However, for the 32 h samples, the W-rich GI precipitates in the Fe–Au–W ternary alloy are much smaller, compared to those in the Fe–W sample. The Au-rich and (Au/W)-rich precipitates are generally larger and show a roundish shape, which are difficult to differentiate without further compositional analysis. After ageing for 100 h, the W-rich precipitates show a branched surface precipitate structure for some of the grains (Fig. 1c). It is clear that there are more W-rich precipitates for some grains (e.g. grain 1) than in others (e.g. grain 2 and 3). Grain 4 in Fig. 1c gives an example in which some roundish Au-rich GI precipitates can be observed, while no W-rich precipitates are found.

A compositional map of the Fe–Au–W sample after ageing for 100 h is shown in Fig. 2. It can be observed

that the grain boundaries are mainly covered by Au-rich precipitates, while the GI branched surface precipitate structures are W-rich. In the interior also Au-rich precipitates can be observed: some are isolated, and some are in contact with the W-rich patterns like snow decorating the branches. From Figs. 1 and 2, by comparing the 100 h Fe–Au–W ternary sample with its binary counterparts, two major differences can be observed: (1) in the grains covered with the branched surface precipitate structures the area fraction of the W-rich precipitates is much larger for the Fe–Au–W sample than that in the Fe–W sample and (2) in the Fe–Au alloy, the Au-rich precipitates show a strong tendency to dissolve and migrate towards the grain boundaries via the diffusion of Au atoms, leaving only small GI precipitates in the grains (Fig. 1f), while in the Fe–Au–W alloy, large Au-rich GI precipitates are found in the majority of the examined grains.

A closer observation of the (Au/W)-rich GI particles yields more detailed information. Figure 3 shows the GI precipitates for the ternary Fe–Au–W alloy

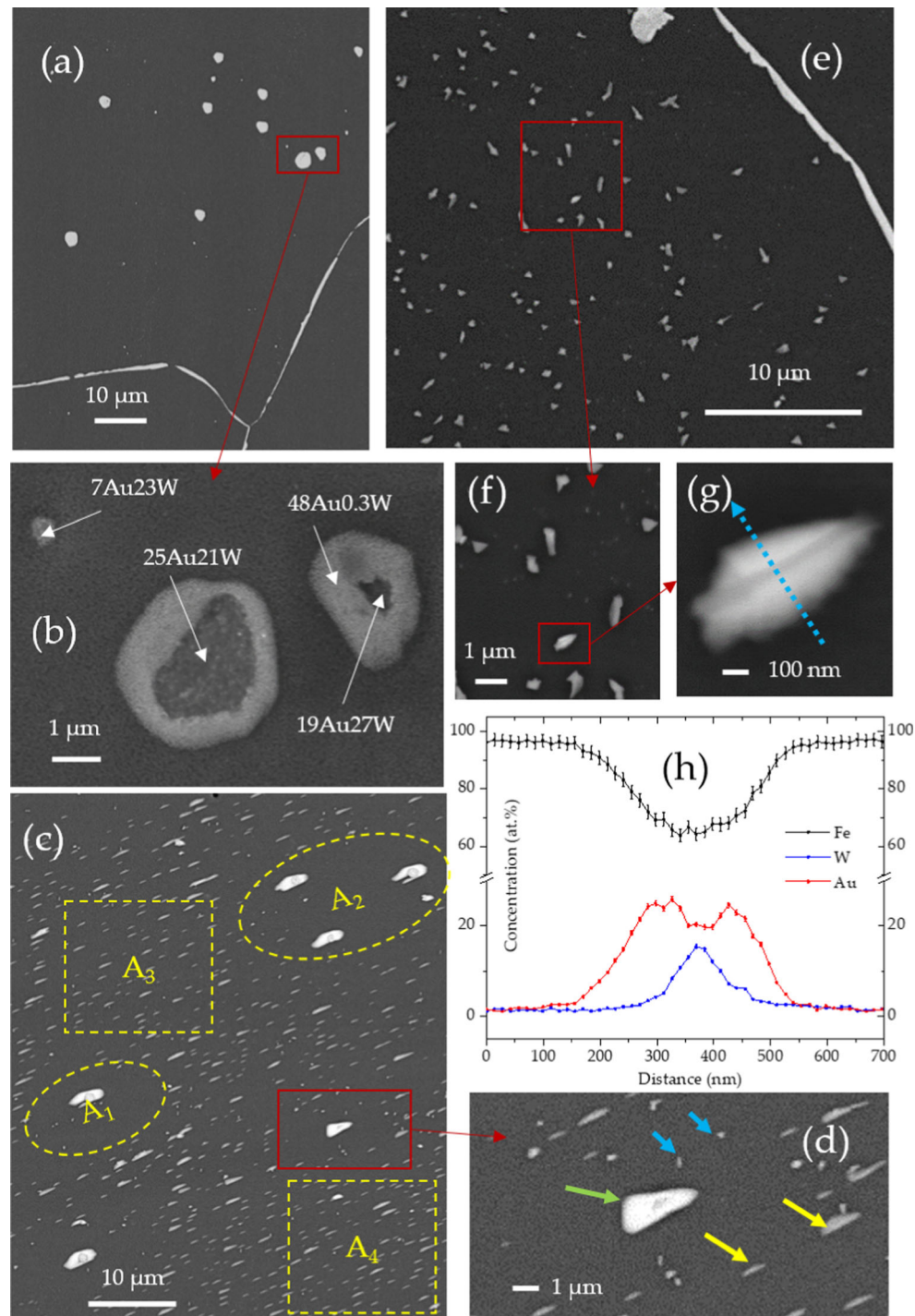


Figure 3 SEM images for the Fe–Au–W sample after ageing for 32 h. **a, b**: Morphology and structure of the (Au/W)-rich GI precipitates; **c, d** Effect of the (Au/W)-rich precipitates on the

after ageing for 32 h. The roundish precipitates in Fig. 3a are either enriched in Au or enriched in both Au and W. A SEM image with higher magnification is provided in Fig. 3b. The small precipitate at the top

distribution of the Au-rich GI precipitates. **e–g** Au-rich and W-rich GI precipitates form in contact to each other, yielding a sandwich structure; **h** Compositional scan along the line in (g).

left corner is enriched in both Au and W, while the two larger particles show a core–shell structure. The cores of the particles are enriched in both Au and W, while the shells are enriched in Au only. It is

therefore inferred that the W-rich precipitates formed first, while the Au-rich precipitation is added from below, and subsequently wrapped the previously-formed W-rich particles, eventually forming a core-shell structure. There are three types of GI precipitates in Fig. 3c and d: the ones enriched in Au (indicated by yellow arrows), the ones enriched in W (indicated by blue arrows) and the ones with a core-shell structure (indicated by a green arrow). In Fig. 3c, it is observed that the majority of the Au-rich GI precipitates are uniformly distributed, but in the vicinity of a core-shell particle, a Au depletion zone is generated. In the depletion zone, only W-rich precipitates can be observed, which indicates that the Au-rich precipitates show a higher mobility on the free surface compared to their W-rich counterparts.

Similar to the grain boundaries, the precipitates with a core-shell structure also act as a sink (or assembly site) for the Au-rich precipitates. This explains the difference in size distribution of the Au-rich precipitates between the ternary Fe–Au–W alloy and the binary Fe–Au alloy for long ageing times. In the Fe–Au alloy only, the grain boundaries act as a sink for the Au-rich precipitates, and therefore most of the Au-rich GI precipitates are collected by the grain boundaries after 100 h of ageing. In the Fe–Au–W alloy, however, both the grain boundaries and the core-shell particles act as assembly sites for the Au-rich precipitates, and as a result some GI precipitates have survived the long-term ageing in the form of core-shell particles. It is worth noting that compared to the uniformly distributed Au-rich precipitates, the precipitates attracted by the assembly sites cover a smaller area fraction. For example, the area fraction of the Au-rich precipitates in regions A₃ and A₄ in Fig. 3c is about twice as high as in regions A₁ and A₂. This strongly suggests that the precipitates thicken during the coarsening. Figure 3e–h may correspond to the early stage of the core-shell structure formation. In Fig. 3g, it is observed that Au-rich precipitates form from both sides of a previously-formed W-rich precipitate, resulting in a sandwich-like structure. This observation of side-by-side formation is consistent with the results from creep-failed samples [17], where Au-rich and W-rich precipitated are found to be present in contact with each other (without forming a compound).

It is worth to note that a core-shell structure was also observed in [19], however, different mechanisms account for the structures in the two studies. In

reference [19], the core-shell structure was due to the temperature change during cooling and the associated changes in the equilibrium Ge concentration, while in the current study, the core-shell structure results from the Au diffusion towards the pre-existing W-rich particles, which act as nucleation sites.

To investigate how far the precipitates extend below the surface into the matrix, a plasma focused ion beam (PFIB) was used to further investigate the Fe–Au–W alloy after 100 h of ageing, as shown in Fig. 4. As indicated in Fig. 4a, three cross-sectional slits were generated containing the W-rich precipitates (Fig. 4b and c) and the Au-rich grain boundary (Fig. 4d). W-rich precipitates form on the free surface, with an average thickness of about 74 nm (Fig. 4b and c). The matrix precipitates (indicated by the yellow arrows) are Au-rich precipitates. Our previous research [6, 7] revealed that these precipitates have a disc-shaped geometry and are generally connected to dislocations. In Fig. 4d, a valley filled with Au-rich precipitation along the grain boundary can be observed, with a width of about 1.4 μm and a depth of about 0.9 μm. Au-rich precipitation is also observed on the grain boundary underneath the free surface, suggesting that Au transport primarily proceeds via (1) diffusion along the grain boundaries underneath the surface and (2) surface diffusion. The diffusion paths of the Au atoms are indicated by the green arrows in Fig. 4d. It is worth noting that W-rich precipitates are also observed on the Au-covered grain boundary (indicated by a blue arrow in Fig. 4d and e), indicating a segregation tendency of W solutes towards the grain boundaries. However, the solute Au shows a much stronger segregation tendency towards the grain boundaries compared to solute W.

To our knowledge, the Fe–Au–W ternary phase diagram has not yet been measured or calculated. However, given the immiscibility and the positive formation energy for the Au–W system [20, 21], and the fact that the Au-rich and W-rich precipitates form independently instead of forming a compound [17], the phases of the Au-rich and W-rich precipitates were estimated on the basis of the binary phase diagrams for Fe–Au and Fe–W systems, respectively. According to the binary phase diagrams, the Au-rich precipitates should show *fcc* structure with 60 at.% Au and 40 at.% Fe at 700 °C, while the W-rich precipitates should correspond to the Fe₂W Laves phase with a hexagonal structure. The phases of the

Figure 4 PFIB-SEM results for the Fe–Au–W alloy after ageing for 100 h. **a** The three locations where PFIB was performed; **b** and **c** The cross-section of W-rich precipitates; **d** and **e** the cross-section of an Au-rich grain boundary. The yellow arrows, blue arrow and green arrows indicate the Au-rich matrix precipitates, W-rich precipitate segregated on a grain boundary and the diffusion paths of Au, respectively.

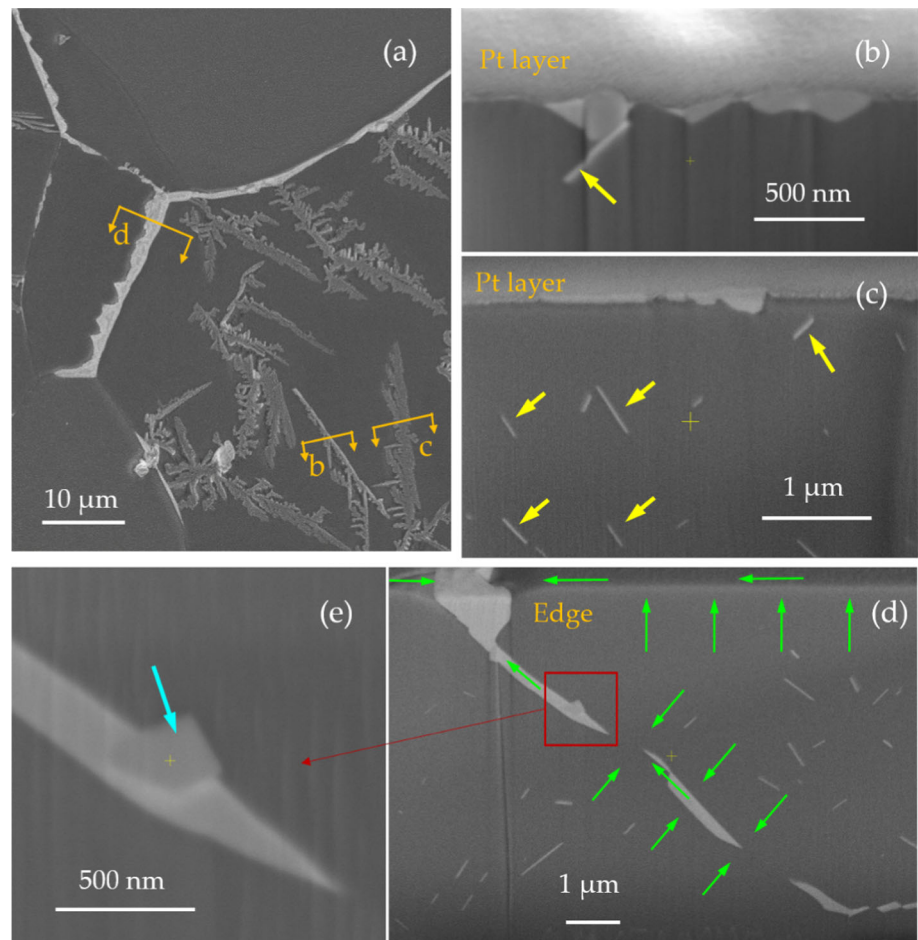
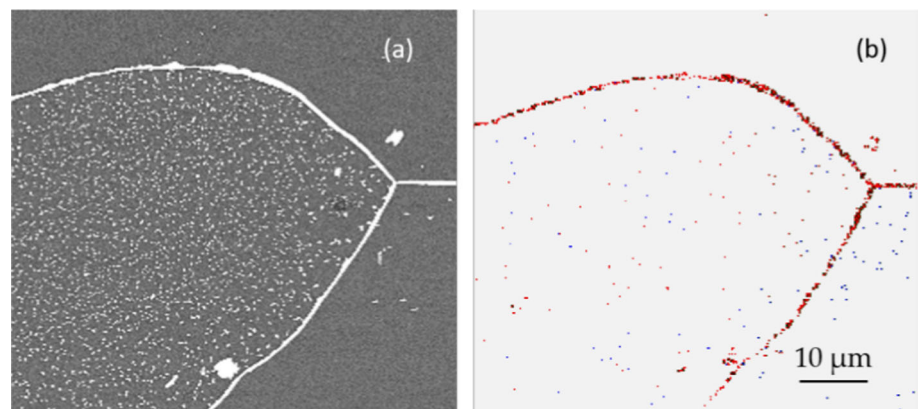


Figure 5 Backscattered electron image **a** and EBSD phase map **b** for a Fe–Au–W sample after 32 h of ageing. The red corresponds to the *fcc* Au phase, while the blue corresponds to the hexagonal Fe_2W Laves phase.



precipitates were determined by EBSD as shown in Fig. 5. The red and blue colours correspond to the *fcc* Au phase and the hexagonal Fe_2W Laves phase, respectively. In the current research, the Au-rich precipitates show a Au concentration of 40–60 at.%, while the W-rich precipitates show a W concentration of 20–32 at.%, which is consistent with the expected composition within the accuracy of the EDS. The

particles enriched in both Au and W (see Fig. 3b), a particle has 7 at.% Au and 23 at.% W) correspond to a situation where the Au-rich and W-rich precipitates are formed in contact to each other (instead of forming a ternary compound), but due to the spatial resolution limitation of EDS, we cannot separate them.

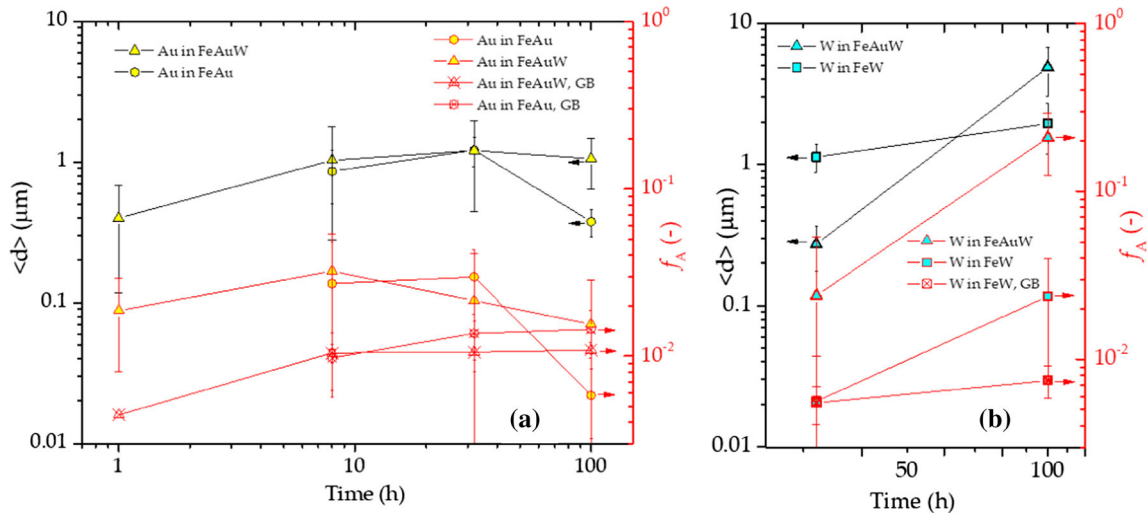


Figure 6 Equivalent diameter of the GI precipitates and area fraction of both the GB and GI precipitates for **a** the Au-rich precipitation in Fe–Au–W and Fe–Au alloys and **b** the W-rich precipitation in Fe–Au–W and Fe–W alloys for different ageing times.

To quantify the precipitation in the three alloys, and thus compare the precipitates in the ternary alloy with its binary counterparts, in Fig. 6 the equivalent diameter (for the GI precipitates) and the area fraction (for the sum of the GI and GB precipitates) are presented for the three alloys as a function of the ageing time. For each sample, 7 to 15 grains were analysed, and the average value and the scatter are shown. The Au-rich and W-rich precipitates are presented separately for clarity. The results of Fig. 6a indicate that: (1) the equivalent diameter of the GI precipitates increases up to about 32 h for both the Fe–Au–W and Fe–Au alloys. However, from 32 to 100 h, the size of the GI precipitates in the Fe–Au–W alloy remains about constant, while in the Fe–Au alloy the GI precipitates show a significant decrease in size. (2) the area fraction of the GI precipitates for the Fe–Au alloy increases slightly from 8 to 32 h before it decreases significantly from 32 to 100 h, indicating a significant Au diffusion towards the grain boundaries. For the Fe–Au–W alloy, the area fraction peaks at 8 h before it decreases gradually from 8 to 100 h. The decrease in area fraction occurs earlier in the Fe–Au–W ternary alloy, because there are more assembly sites (the precipitates with the core–shell structure) for the Au-rich GI precipitates. With the diffusion of Au, some Au-rich precipitates grow at the expense of the others dissolving, resulting in a smaller area fraction. (3) the grain boundaries of the Fe–Au alloy collect more Au-rich GI precipitates compared to the ternary Fe–Au–W counterpart,

as can be seen from the area fraction of the GB precipitates. This is consistent with the results in Fig. 1: in the Fe–Au alloy most of the Au-rich GI precipitates are collected by the grain boundaries after 100 h ageing, while in the ternary Fe–Au–W system the particles with a core–shell structure provide extra assembly sites for the Au-rich GI precipitates.

The size and the area fraction of the W-rich precipitates in Fe–Au–W and Fe–W alloys are compared in Fig. 6b. Unlike the fast size evolution of the Au-rich GI precipitates that results in a maximum size around 32 h, the W-rich GI precipitates are still growing from 32 to 100 h. The W-rich GI particles are smaller in size in the Fe–Au–W alloy at 32 h, but the smaller particles show a larger area fraction compared to their counterparts in the Fe–W alloy. During the whole ageing process, the area fraction of the W-rich precipitates in the ternary Fe–Au–W alloy is 5–10 times larger than that in the binary Fe–W alloy. It is also worth noting that from 32 to 100 h, the area fraction of the GI precipitates in the Fe–W alloy increased by 5 times, while the area fraction of the GB precipitates remains at a relative constant level. This indicates that the surface diffusion of W is much slower than that of Au, so that the Au-rich GI precipitates on the surface show an obvious tendency to migrate towards the grain boundaries (and to the core–shell structures) via the Au atom diffusion, while the W-rich precipitates tend to be immobile once formed on the surface.

As indicated in Fig. 6b, the Au segregation clearly enhances the precipitation kinetics of the W-rich Fe₂W Laves phase on the surface. This is expected to be caused by the enhanced W diffusion in the matrix and an enhanced nucleation in the ternary Fe–Au–W alloy, as the solute Au depleted diffusion layer below the surface shows a significant shrinkage. From Fig. 6b, it is clear that at 100 h the surface fraction for the Fe₂W precipitates in the ternary Fe–Au–W alloy ($f_A \approx 21\%$) is one order of magnitude larger compared to that in the binary Fe–W alloy ($f_A \approx 2\%$). This indicates a much slower kinetics. In fact, the value of the surface fraction f_A observed for the binary Fe–W alloy at 100 h is of the same order as the surface fraction f_A for the ternary Fe–Au–W alloy at 32 h ($f_A \approx 2\%$). As shown in Fig. 1, for the ternary Fe–Au–W alloy at 32 h also no branched structure was observed, consistent with the observation for the binary Fe–W alloy at 100 h. It is therefore expected that the branched structure in the binary Fe–W alloy is only formed for a larger surface fraction f_A , which is expected to be reached for significantly longer times (about 400 h). The origin for the transition in morphology from roundish to branched surface precipitates has not been established, but is expected to be related to an anisotropy in growth rate with respect to orientation. As the hexagonal Fe₂W Laves phase has a significantly lower symmetry than the *bcc* Fe-based matrix the most favourable growth conditions are expected for specific orientation relations between the precipitate and the matrix (for which the interfacial strain is minimised). In TEM studies, on bulk Fe–Cr–Co–W steels three different orientation relations (OR1: $[10\bar{1}]_\alpha \parallel [\bar{1}2\bar{1}1]_{L'}$, $(111)_\alpha \parallel (\bar{1}10\bar{3})_{L'}$, $(011)_\alpha \parallel (0001)_L$; OR2: $[\bar{1}\bar{1}3]_\alpha \parallel [2\bar{1}\bar{1}0]_{L'}$, $(1\bar{1}0)_\alpha \parallel (01\bar{1}3)_{L'}$, $(4\bar{1}1)_\alpha \parallel (0001)_L$; and OR3: $[011]_\alpha \parallel [2\bar{1}\bar{1}0]_{L'}$, $(100)_\alpha \parallel (02\bar{2}3)_{L'}$, $(\bar{1}\bar{1}\bar{1})_\alpha \parallel (0001)_L$) have been identified for the hexagonal Fe₂W Laves phase (*L*) precipitates and the α -Fe matrix (α) [22]. These orientations relations are expected to also govern the branching growth behaviour of the Fe₂W surface precipitates on the *bcc* Fe matrix.

Discussion

The evolution of the size and site density of grain-interior precipitates

The size and distribution of the GI precipitates in every analysed grain are provided in Fig. 7. Each data point corresponds to the information from a single grain. The Au-rich and W-rich precipitates in the Fe–Au–W alloy are considered separately. Since it is difficult to classify the Au-rich and (Au/W)-rich particles unambiguously just by their shape, the roundish particles with a core–shell structure (Fig. 3b) are regarded as Au-rich precipitates. Assuming that the ratio between the GB precipitation and the GI precipitation is constant in each grain after a fixed annealing time, then the total amount of the GI precipitates per unit area is the same for each grain. If all precipitates have a constant thickness, then the area fraction of precipitates shows a scaling relation $n_A \propto \langle d \rangle^m$ with a slope of $m = -2$. If the precipitates are shape-conserved, then the particles grow in three directions and their thickness is proportional to the corresponding equivalent diameter, resulting a scaling relation $n_A \propto \langle d \rangle^m$ with a slope of $m = -3$.

For a grain area S_G , a number of precipitates N , and a particle average diameter $\langle d \rangle$, the number density n_A and the area fraction f_A of the GI precipitates correspond to $n_A = N/S_G$ and $f_A = N(\pi/4)\langle d^2 \rangle / S_G \approx N(\pi/4)\langle d \rangle^2 / S_G = (\pi/4)\langle d \rangle^2 n_A$. The dashed lines in Fig. 7 with a slope of $m = -2$ correspond to 0.1%, 1% and 10% area fraction contours, respectively. Assuming an average GI precipitate height $\langle h \rangle$ that is proportional to its equivalent diameter $\langle d \rangle$ with a scaling factor A , then the total volume V_G of the GI precipitates per unit area S_G (the equivalent thickness of the precipitation layer on the surface if the precipitates spread over the sample surface, covering it uniformly) corresponds to $a = V_G/S_G \approx (NA\langle d \rangle^3) / (N/n_A) = A\langle d \rangle^3 n_A$. The scaling factor A depends on the GI precipitate shape. The solid lines in Fig. 7 with a slope of $m = -3$ correspond to an equivalent thickness of 0.1, 1 and 10 nm, respectively ($A = \pi/20$, for a cylinder-shaped particle with a height of $0.2 \langle d \rangle$ [18]).

As indicated in the schematic diagram inserted Fig. 7a, it is easy to determine whether the GI

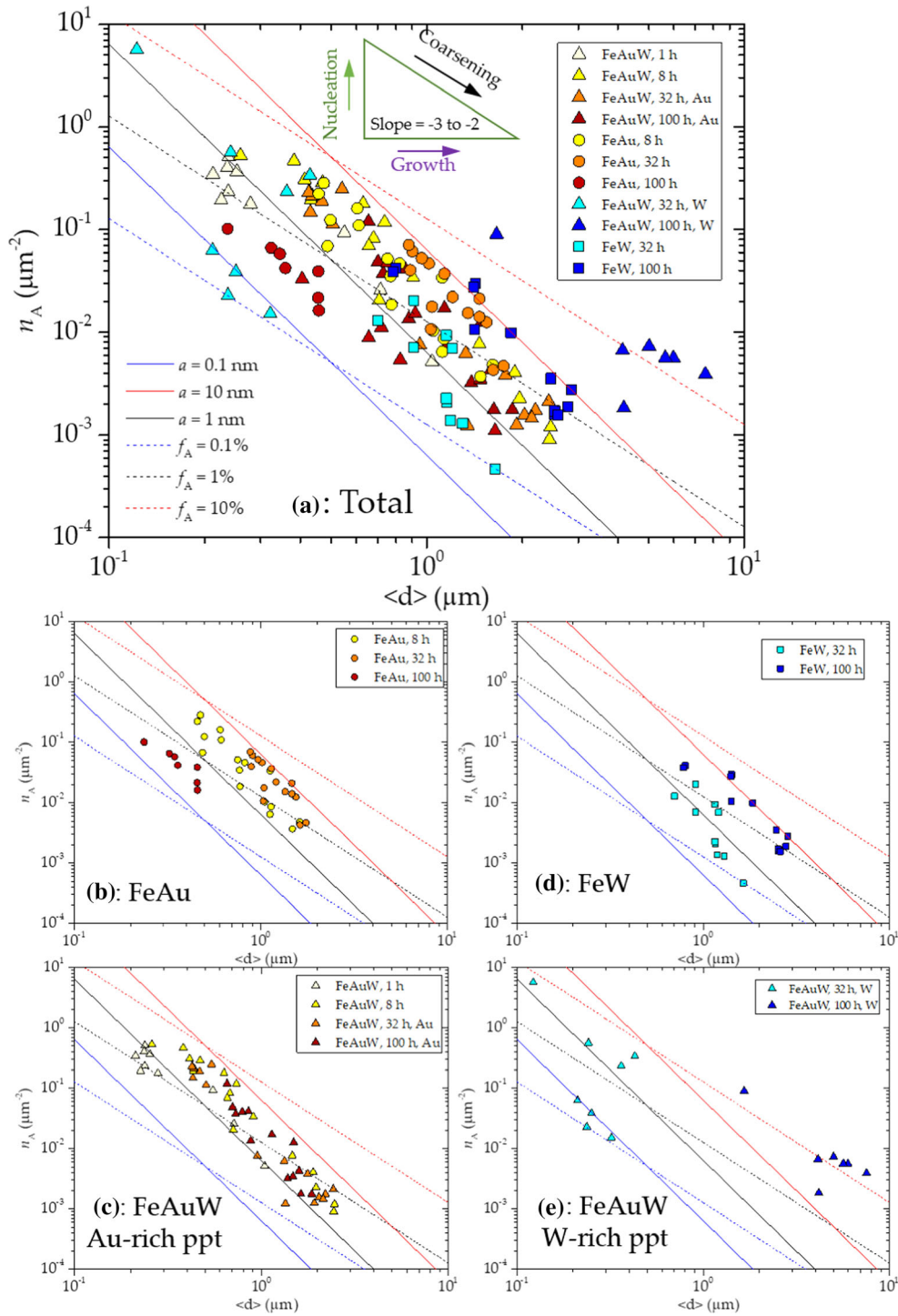


Figure 7 Map of the number density n_A versus the average size $\langle d \rangle$ of the GI precipitates in each grain of the three alloys after different ageing times. **a** Summary all the data. **b–e** Individual maps for: **b** Au-rich precipitates in the Fe–Au alloy, **c** Au-rich precipitates in the Fe–Au–W alloy, **d** W-rich precipitates in the Fe–

W alloy and **e** W-rich precipitates in the Fe–Au–W alloy, respectively. The dashed straight lines correspond to $n_A \propto \langle d \rangle^{-2}$ scaling behaviour (constant thickness) and the solid lines to $n_A \propto \langle d \rangle^{-3}$ scaling behaviour (shape conservation).

precipitates are in the stage of nucleation, growth, coarsening or a combination. For instance, if the precipitates experienced an increase in number density without a change in their size (as indicated by the upward pointing green arrow), then the particles are in the nucleation stage. If the number density keeps constant and the size increases, then the precipitates are growing (indicated by the right pointing purple arrow). A constant area fraction (or equivalent thickness) with an increase in size and a decrease in number density corresponds to a coarsening process (indicated by the black arrow).

The size and distribution of the GI Au-rich precipitates for the Fe–Au alloy after ageing for 8, 32 and 100 h, respectively, are shown in Fig. 7b. By comparing the 8 and 32 h data, it is clear that the collection of the data points shifted towards the right bottom direction, indicating a typical coarsening process. From 32 to 100 h, the number density of the precipitates remains around the same level, yet the average size and the corresponding area fraction and equivalent thickness decreased significantly, resulting from the diffusion of the Au solute towards the grain boundaries. For all the three ageing times, the data points closely follow a $n_A \propto \langle d \rangle^m$ scaling with a slope m of $-3.2(3)$ at 8 h, $-3.1(6)$ at 32 h and $-2.3(5)$ at 100 h. It is therefore indicated that for shorter ageing times (≤ 32 h), the GI precipitates in the Fe–Au system are likely to be shape-conserved, while after ageing for 100 h, the thickness of the precipitates seems to approach a constant value.

The characteristics of the Au-rich GI precipitates in the Fe–Au–W alloy are shown in Fig. 7c. At an ageing time of 1 h, most of the precipitates have an equivalent diameter smaller than $0.3 \mu\text{m}$, but the equivalent diameter of the largest precipitate already exceeded $1 \mu\text{m}$, indicating that growth had occurred in some grains. From 1 to 8 h, the precipitates experience an obvious growth, and the precipitate area fraction and equivalent thickness are similar in all the grains (also similar to the Fe–Au counterpart). The precipitation behaviour in the Fe–Au–W alloy after ageing for 32 and 100 h is very different from the observation in the Fe–Au alloy. Firstly, the precipitate size and number density show a wider distribution. In addition, the decrease in area fraction and equivalent thickness only occurred in limited number of grains. This is consistent with the observation in Fig. 1d, where several large GI particles remained after 100 h

of ageing (probably in the form of a core–shell structure). From 1 to 100 h, the data points follow a $n_A \propto \langle d \rangle^m$ scaling with a slope m of $-2.4(3)$ at 1 h, $-3.0(2)$ at 8 h, $-3.2(2)$ at 32 h and $-2.5(5)$ at 100 h of ageing. This indicates that the precipitation behaviour of the Au-rich is similar for the Fe–Au–W and the Fe–Au alloys.

As shown in Fig. 7d, for the W-rich precipitates in the Fe–W alloy, from 32 to 100 h, the GI precipitates increase both in size and number density with ageing time, indicating a combined nucleation and growth process. For the Fe–Au–W alloy shown in Fig. 7e most of the W-rich precipitates after 32 h ageing have the diameter between 0.2 and $0.4 \mu\text{m}$, while their number densities vary by nearly two orders of magnitude. This indicates that the W-rich precipitates are in the nucleation stage. The data points for the Fe–W alloy follow a $n_A \propto \langle d \rangle^m$ scaling with a slope m of $-4(1)$ at 32 h and $-2.6(3)$ at 100 h. Compared to the binary Fe–W alloy, the W-rich precipitates in the ternary Fe–Au–W alloy are much smaller in size (for 32 h of ageing), but their area fraction is either similar to or nearly one order of magnitude larger than the precipitate area fraction in the Fe–W system. This is consistent with the W-rich precipitation behaviour in the creep-failed samples [17]: the W-rich particles are smaller in the Fe–Au–W alloy than in the Fe–W alloy, but the total amount of the W-rich precipitates is not suppressed. On the contrary, the W-rich precipitation in the Fe–Au–W alloy seems to be accelerated after long-time ageing: for the 100 h samples, the W-rich precipitates show an average area fraction of about 21% with an average height of about 74 nm (see Fig. 4), yielding an equivalent thickness of about 15 nm. Both the area fraction and the equivalent thickness in the Fe–Au–W alloy are much larger than that for the Fe–W alloy. Compared to the Au-rich precipitates, the W-rich precipitates show different growth mechanism: after 100 h of ageing, the W-rich precipitates in the Fe–Au–W sample follow a $n_A \propto \langle d \rangle^m$ scaling with a slope m of $-2.1(6)$, indicating that the W-rich precipitates are plate-shaped with a relatively constant thickness. Two examples are provided in Fig. 8, where the W-rich precipitates with different in sizes and number densities in the two grains yield similar area fractions. The lateral growth of the branched surface precipitates stops when the branches are about to make contact. Since the individual branched surface precipitates are sometimes difficult

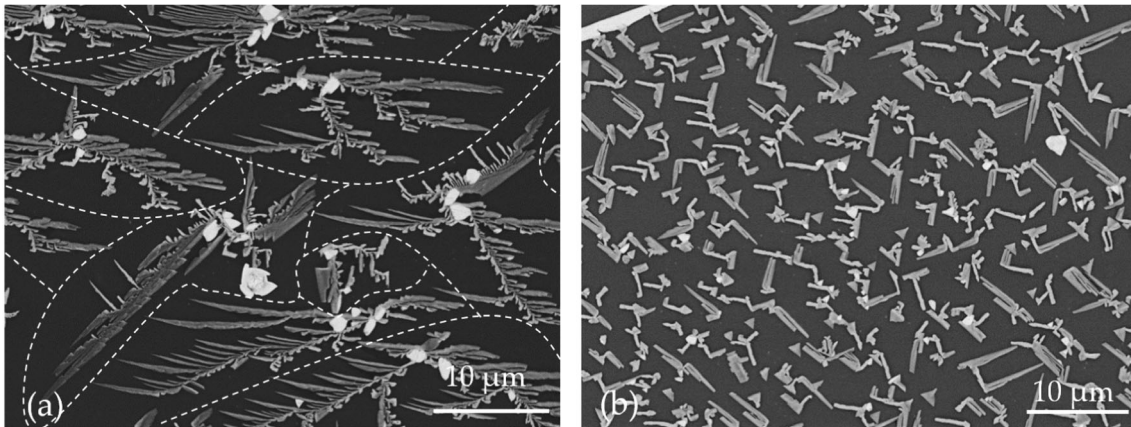


Figure 8 Two examples of W-rich GI precipitates in the Fe–Au–W alloy for an ageing time of 100 h. The equivalent sizes (5.0 and 1.7 μm in **a** and **b**, respectively) and number densities of the W-rich precipitates (0.0073 and 0.0900 μm⁻² in **a** and **b**,

respectively) are obviously different in the two grains, while the area fractions are similar (22 and 24% in **a** and **b**, respectively). The dashed lines in **a** show the partitions of precipitates.

to distinguish (indicated in Fig. 8(a)), in the grains where they are formed, the number density of the precipitates may have been underestimated and the equivalent size overestimated.

The evolution of the equivalent thickness of the grain-interior precipitates

The number density n_A and equivalent diameter $\langle d \rangle$ show for most of the GI precipitates a $n_A \propto \langle d \rangle^m$ scaling with a slope m of about -3, indicating a 3D shape conserving growth and coarsening (see Fig. 7). It is therefore easy to obtain the equivalent thickness attributed by the GI precipitates by fitting the data in Fig. 7 with a fixed slope of $m = -3$ (assuming $A = \pi/20$).

$$a \approx A \langle d \rangle^3 n_A \tag{1}$$

For the W-rich precipitates in the Fe–Au–W alloy after 100 h of ageing, fitting by Eq. (1) yields an equivalent thickness of 102 nm. Since the branched surface precipitates seem to have a constant thickness (as discussed in Sect. “The evolution of the size and site density of grain-interior precipitates”), the equivalent layer thickness of the W-rich precipitates is estimated by $a_W \approx h f_A$. After 100 h of ageing, the average height of the W-rich precipitates corresponds to $h = 74$ nm.

The surface precipitation of the solutes can be simplified into a 1D diffusion process, where the solute agents diffuse towards the free surface, and after reaching the surface they nucleate to form

precipitates. The 1D flux and the equivalent thickness of the precipitation layer are estimated by [23]:

$$J_X = \frac{D_X \Delta x}{\Omega} \left(\frac{1}{\sqrt{\pi D_X t}} \right) = \frac{\Delta x}{\Omega} \sqrt{\frac{D_X}{\pi t}} \tag{2}$$

and

$$a(t) = \frac{\Omega}{x_p} \int_0^t J_X(a, t') dt' = \frac{\Delta x}{x_p} \sqrt{\frac{4 D_X t}{\pi}} \tag{3}$$

where $\Delta x = x_\infty - x_1$ is the supersaturation of the solute element X, D_X is the diffusivity of the solute element in the matrix phase, Ω is the atomic volume, t is the time and x_p is the concentration of the solute element in the precipitate phase.

The experimental results estimated by Eq. (1) and the results calculated by Eqs. (2) and (3) are compared in Fig. 9. The Au-rich GI precipitates show a similar trend in the ternary Fe–Au–W alloy as in the binary Fe–Au alloy. In the early stage (before 32 h for the Fe–Au sample and 8 h for the Fe–Au–W system), the thickness of the Au-rich GI precipitates shows an increase $a \propto t^\alpha$ with a slope α of approximately 0.5, indicating a diffusion-controlled process. For the W-rich precipitates, the corresponding slope α is much larger than 1/2, indicating that the W-rich precipitates are still in the nucleation stage. Compared to the W-rich GI particles in the binary Fe–W alloy, the precipitates in the ternary Fe–Au–W alloy starts with a smaller size and a higher number density n_A , yielding a lower equivalent thickness. After ageing for 100 h, however, the thickness of the W-rich

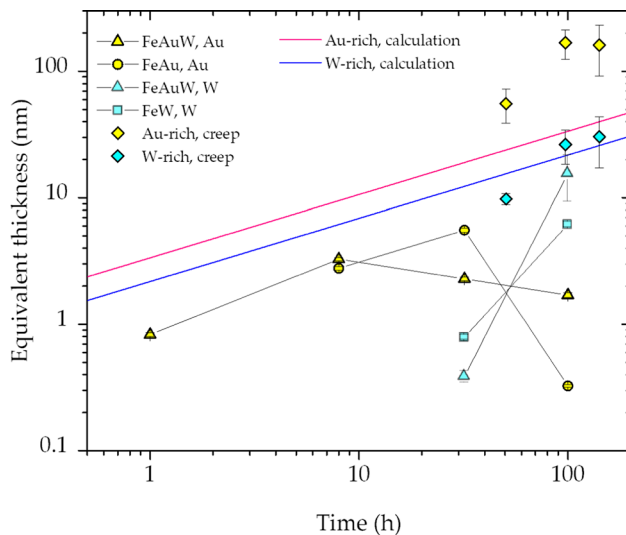


Figure 9 Equivalent thickness of the GI precipitation layer a for the three alloys as a function of ageing time t . The solid lines are calculated by $a(t) = (2/\sqrt{\pi})(\Delta x/x_p)\sqrt{D_X t}$, where Δx is the supersaturated solute fraction, x_p the solute fraction in the precipitate and D_X the solute (volume) diffusivity of element X . The experimental data are obtained from Fig. 7 assuming $n_A \propto \langle d \rangle^{-3}$. The scattered data points are creep results from a previous research on Fe–Au–W system [17].

precipitation in the Fe–Au–W system exceeded that in the Fe–W system by nearly three times, indicating that the W diffusion in the Fe–Au–W system is accelerated for longer ageing times. The acceleration phenomenon may result from the depletion of supersaturated Au solute. At 700 °C, the diffusivity of Au is two orders of magnitude higher than that of W, so that the depletion of Au is much faster. With the diffusion of Au towards the surface, a shrinkage is generated in the Au-depleted matrix, due to the size difference between the Au and Fe atoms. The resulting elastic tensile strain field may cause an enhanced diffusion of W [24].

The scattered data on the right top corner corresponds to the equivalent thickness of the particles from the creep experiment [17]. The creep experiments were performed at 550 °C. For comparison, the data in Fig. 9 were normalised using Eq. (3), i.e. by applying a scaling factor $a^{T_1}/a^{T_2} = \left(x_p^{T_2} \Delta x^{T_1} \sqrt{D_X^{T_1}}\right) / \left(x_p^{T_1} \Delta x^{T_2} \sqrt{D_X^{T_2}}\right)$. It is clear that the equivalent thicknesses of both the Au-rich and W-rich precipitates are systematically higher under the creep conditions. Two reasons are expected to be responsible for the difference: (1) During creep a

significant amount of excess vacancies and dislocations are generated by the deformation [25, 26], which enhances the diffusion of the solutes. (2) for surface precipitation only a fraction of the solutes diffuses towards the grain-interior free surface directly, as the rest of the solutes are attracted by the nearby grain boundaries, through which the solutes can reach the free surface (indirect route with different diffusion rates). Assuming the solutes choose the shortest diffusion path (to either the nearest grain boundary or the nearest free surface), then GI precipitates would no longer form after the diffusion length reaches half of the grain size. For average grain sizes of 84 μm (Fe–Au sample) and 105 μm (Fe–Au–W sample), the newly-nucleated Au-rich GI precipitates are not expected to form any longer after about 500 h and 800 h ageing, respectively.

Linking the surface precipitation to the creep cavity precipitation

The external free surface precipitation bears great resemblance to the formation of precipitates on the surface of the internal creep cavities as formed in creep experiments. In a previous study on the Fe–Au system [18], the growth rate of the Au-rich precipitates on the external free surface was found to be comparable to that on the internal free surface of a creep-induced cavity. By comparing the present study with the creep results for the Fe–Au–W alloy [17], similarities are observed in terms of the size and distribution of the precipitates and the interplay between the two solutes. In the Fe–Au–W alloy, the Au-rich and W-rich precipitates are found to form in contact to each other, yielding a sandwich-like structure, for surface conditions (present work) and for creep conditions (ref. [17]). In the Fe–Au–W alloy and the Fe–Au alloy, the evolution of the Au-rich GI precipitates (the ones not connected to grain boundaries) is similar, indicating that the addition of W does not seem to have a strong influence on the kinetics of solute Au. Similar results were obtained under the creep conditions, where the size evolution of the Au-rich precipitates is comparable in the Fe–Au–W alloy [17] and the Fe–Au alloy [13]. The precipitation behaviour of the W-rich GI precipitates is, however, significantly different in the Fe–Au–W alloy compared to the Fe–W alloy. In the present research, it is observed that the W-rich GI precipitates in the Fe–Au–W alloy start with a smaller size and larger

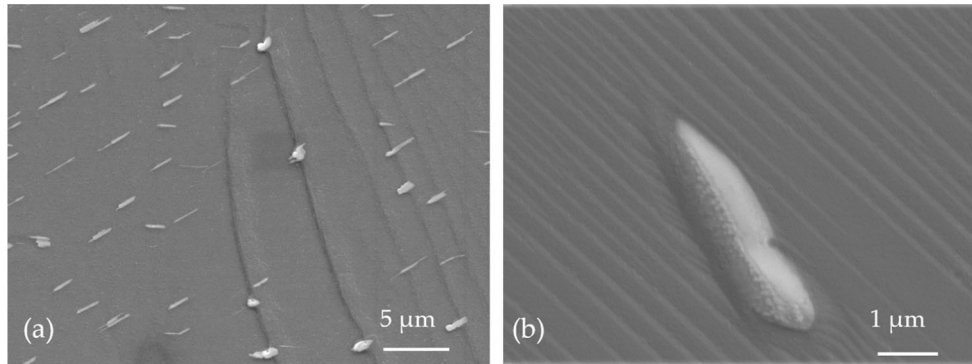


Figure 10 Terraces generated after the nucleation of Au-rich GI precipitates on the surfaces of **a** Fe-Au and **b** Fe-Au-W alloy samples.

number density, but the overall diffusion flux is not reduced for longer ageing times. The creep experiments show similar results: the W-rich precipitates formed in the creep-induced cavities show smaller sizes and a higher number density in the Fe–Au–W alloy [17] compared to the Fe–W alloy [12], indicating that more nucleation sites are available for W-rich precipitation in the Fe–Au–W alloy (both under surface and creep conditions). One explanation may be the increased roughness that is generated with the depletion of the supersaturated Au solute from the underlying matrix. As discussed in “The evolution of the equivalent thickness of the grain-interior precipitates” section, the continuous depletion of Au results in a shrinkage of the matrix and strains resulting from local gradients in the solute Au concentration, which further leads to a re-organisation of the surface atoms into terraces (examples are shown in Fig. 10). Therefore, more nucleation sites are available for the W-rich precipitates in the ternary system, which causes a higher nucleation rate together with the enhanced diffusivity. An estimation of the healing kinetics in [17] also indicated that the W diffusion is not suppressed in the relevant creep cavities.

One difference between the surface precipitation and the creep-cavity precipitation is the shape of the precipitates. Under surface conditions, the aspect ratio of the Au-rich GI precipitates varies from 1.2 (nearly round) to about 12, while for the Fe–Au–W alloy the W-rich GI precipitates develop into branched surface precipitates after long ageing. However, under creep conditions, the shapes of both the Au-rich and W-rich precipitates are constrained by the shape of the creep cavity, so that the Au-rich precipitates with a high aspect ratio and the W-rich branched surface precipitates are not likely to form.

Another difference between the two conditions is the diffusivity of the solutes. As indicated in Fig. 9 and discussed in “The evolution of the equivalent thickness of the grain-interior precipitates” section the diffusion of both Au and W solutes are enhanced under the creep condition, due to the deformation-induced excess vacancies and dislocations. The overall deformation-enhanced diffusivity of element X (either solute or host) corresponds to [25, 26]:

$$D_X = (1 - g)D_X^V + gD_X^P \\ = (1 - g)D_X^L(1 + x_V^{ex}/x_V^{th}) + gD_X^P \quad (5)$$

in which D_X^L is the lattice diffusivity, D_X^V is the solute diffusivity induced by the vacancies, D_X^P is the dislocation-induced pipe diffusivity, x_V^{ex} is the concentration of the excess vacancies, x_V^{th} is the concentration of the vacancies under thermal equilibrium condition, and the factor g corresponds to the fraction of atoms associated with the pipe. Since the production rate of the excess vacancies is proportional to the strain rate, at the strain rates as low as $(2-7) \times 10^{-5} \text{ h}^{-1}$ [17], the pipe diffusion is mainly responsible for the diffusion enhancement and Eq. (5) can be simplified to $D_X = gD_X^P$. At 823 K (550 °C), the Fe self-diffusivity in *bcc* iron is $1.5 \times 10^{-21} \text{ m}^2\text{s}^{-1}$, while the self-diffusivity along dislocations corresponds to about $10^{-15} \text{ m}^2\text{s}^{-1}$ [27]. For self-diffusion, assuming $g = \pi b^2 \rho$, in which b and ρ are the burger’s vector and the dislocation density, and taken as 2.58 \AA and 10^{14} m^{-2} , respectively. The enhanced diffusivity is then estimated to be about 28 times larger than the lattice diffusivity, resulting in an equivalent thickness of about 5 times bigger than under surface conditions. For higher strain rates (e.g. for the Fe–Au [7, 13] and Fe–W [12] systems) where the diffusion through the excess vacancies can no

longer be neglected, a stronger enhancement in diffusivity may be expected.

Conclusions

The precipitation of supersaturated solutes at free surfaces was studied in a ternary Fe-3Au-4W alloy and two binary Fe-3Au and Fe-4W counterpart alloys. The surface precipitation can be categorised into GI precipitates (not connected to grain boundaries) or GB precipitates. The Au-rich GI precipitates show a 3D shape-conserving growth before they are collected by the grain boundaries, while the W-rich Laves phase precipitates, which are relatively immobile once nucleated on the surface, are found to grow laterally with a relative constant thickness. The Au-rich GI precipitates are similar in terms of their size and kinetics to those for the ternary Fe–Au–W and binary Fe–Au systems. However, the W-rich GI precipitates in the Fe–Au–W system show a smaller starting size, a higher number density and an overall faster kinetics compared to the binary Fe–W system. While the precipitation on the free surface showed an overall slower diffusivity than during creep conditions, the surface precipitation experiments can qualitatively predict the healing of the creep-induced grain boundary cavities in terms of the interplay between multiple solutes in the matrix and the resulting solute diffusivities, precipitate nucleation rates and the precipitate size distributions.

Acknowledgements

The authors thank Haixing Fang and Paula Martin Rojo for assistance with the experimental work. Y. Fu acknowledges the financial support provided by China Scholarship Council (CSC).

Compliance with ethical standards

Conflict of interest The authors declare that they have no conflict of interest.

Open Access This article is licensed under a Creative Commons Attribution 4.0 International License, which permits use, sharing, adaptation, distribution and reproduction in any medium or format, as long as you give appropriate credit to the original author(s) and the source, provide a link to the

Creative Commons licence, and indicate if changes were made. The images or other third party material in this article are included in the article's Creative Commons licence, unless indicated otherwise in a credit line to the material. If material is not included in the article's Creative Commons licence and your intended use is not permitted by statutory regulation or exceeds the permitted use, you will need to obtain permission directly from the copyright holder. To view a copy of this licence, visit <http://creativecommons.org/licenses/by/4.0/>.

References

- [1] Van der Zwaag S (2007) Self healing materials: an alternative approach to 20 centuries of materials science. Springer, Netherlands
- [2] Hager MD, Greil P, Leyens C, van der Zwaag S, Schubert US (2010) Self-healing materials. *Adv Mater* 22(47):5424–5430. <https://doi.org/10.1002/adma.201003036>
- [3] Van Dijk NH, van der Zwaag S (2018) Self-healing phenomena in metals. *Adv Mater Interfaces* 5(17):1800226. <https://doi.org/10.1002/admi.201800226>
- [4] Laha K, Kyono J, Kishimoto S, Shinya N (2005) Beneficial effect of B segregation on creep cavitation in a type 347 austenitic stainless steel. *Scr Mater* 52(7):675–678. <https://doi.org/10.1016/j.scriptamat.2004.11.016>
- [5] Lumley RN, Morton AJ, Polmear IJ (2002) Enhanced creep performance in an Al–Cu–Mg–Ag alloy through underageing. *Acta Mater* 50:3597–3608. [https://doi.org/10.1016/S1359-6454\(02\)00164-7](https://doi.org/10.1016/S1359-6454(02)00164-7)
- [6] Zhang S, Kwakernaak C, Sloof W, Brück E, van der Zwaag S, van Dijk NH (2015) Self healing of creep damage by gold precipitation in iron alloys. *Adv Eng Mater* 17(5):598–603. <https://doi.org/10.1002/adem.201400511>
- [7] Zhang S, Kwakernaak C, Tichelaar FD, Sloof WG, Kuzmina M, Herbig M, Raabe D, Brück E, van der Zwaag S, van Dijk NH (2015) Autonomous repair mechanism of creep damage in Fe–Au and Fe–Au–B–N Alloys. *Metall Mater Trans A* 46(12):5656–5670. <https://doi.org/10.1007/s11661-015-3169-9>
- [8] Lumley RN, Polmear IJ (2007) Advances in self healing of metals. In: Paper presented at the Proceedings of the First International Conference on Self Healing Materials, Noordwijk aan Zee, Netherlands
- [9] Shinya N (2008) Self-healing of metallic materials: self-healing of creep cavity and fatigue cavity/crack. In: Ghosh SK (ed) *Self-healing materials: fundamentals, design strategies, and applications*. Wiley, Hoboken, pp 219–250

- [10] Zhang S, Cizek J, Yao Z, Oleksandr M, Kong X, Liu C, van Dijk NH, van der Zwaag S (2019) Self healing of radiation-induced damage in Fe–Au and Fe–Cu alloys: combining positron annihilation spectroscopy with TEM and ab initio calculations. *J Alloys Comp* 817:152765. <https://doi.org/10.1016/j.jallcom.2019.152765>
- [11] Laha K, Kyono J, Sasaki T, Kishimoto S, Shinya N (2005) Improved creep strength and creep ductility of type 347 austenitic stainless steel through the self-healing effect of boron for creep cavitation. *Metall Mater Trans A* 36a(2):399–409. <https://doi.org/10.1007/s11661-005-0311-0>
- [12] Fang H, Szymanski N, Versteyley CD, Cloetens P, Kwakernaak C, Sloof WG, Tichelaar FD, Balachandran S, Herbig M, Brück E, van der Zwaag S, van Dijk NH (2019) Self healing of creep damage in iron-based alloys by supersaturated tungsten. *Acta Mater* 166:531–542. <https://doi.org/10.1016/j.actamat.2019.01.014>
- [13] Fang H, Versteyley CD, Zhang S, Yang Y, Cloetens P, Ngantillard D, Brück E, van der Zwaag S, van Dijk NH (2016) Autonomous filling of creep cavities in Fe–Au alloys studied by synchrotron X-ray nano-tomography. *Acta Mater* 121:352–364. <https://doi.org/10.1016/j.actamat.2016.09.023>
- [14] He SM, van Dijk NH, Schut H, Peekstok ER, van der Zwaag S (2010) Thermally activated precipitation at deformation-induced defects in Fe–Cu and Fe–Cu–B–N alloys studied by positron annihilation spectroscopy. *Phys Rev B* 81(9):094103. <https://doi.org/10.1103/PhysRevB.81.094103>
- [15] van der Zwaag S, Brinkman E (2015) Self healing materials: pioneering research in the Netherlands. IOS Press, Amsterdam
- [16] Zhang S, Fang H, Gramsma ME, Kwakernaak C, Sloof WG, Tichelaar FD, Kuzmina M, Herbig M, Raabe D, Brück E, van der Zwaag S, van Dijk NH (2016) Autonomous filling of grain-boundary cavities during creep loading in Fe–Mo alloys. *Metall Mater Trans A* 47(10):4831–4844. <https://doi.org/10.1007/s11661-016-3642-0>
- [17] Fu Y, Kwakernaak C, Sloof WG, Tichelaar FD, Brück E, Van der Zwaag S, van Dijk NH (2020) Competitive healing of creep-induced damage in a ternary Fe–3Au–4W alloy. *Metall Mater Trans A* 51:4442–4455. <https://doi.org/10.1007/s11661-020-05862-6>
- [18] Sun WW, Fang H, van Dijk NH, van der Zwaag S, Hutchinson CR (2017) Linking surface precipitation in Fe–Au alloys to its self-healing potential during creep loading. *Metall Mater Trans A* 48(5):2109–2114. <https://doi.org/10.1007/s11661-017-4025-x>
- [19] Chen Y, Fang XY, Brechet Y, Hutchinson CR (2014) Surface precipitation on engineering alloys. *Acta Mater* 81:291–303. <https://doi.org/10.1016/j.actamat.2014.08.044>
- [20] Vijayakumar H, Sriramamurthy AH, Nagender Naidu SV (1988) Calculated phase diagrams of Cu–W, Ag–W and Au–W binary systems. *Calphad* 12:177–184. [https://doi.org/10.1016/0364-5916\(87\)90034-4](https://doi.org/10.1016/0364-5916(87)90034-4)
- [21] Zhang R-F, Shen Y-X, Kong L-T, Lai W-S, Liu B-X (2004) Metastable phase selection of an immiscible Au–W System studied by ab initio calculation, molecular dynamics simulation and ion-beam mixing. *Jpn J Appl Phys* 43:7648–7653. <https://doi.org/10.1143/jjap.43.7648>
- [22] Yamamoto K, Kimura Y, Mishima Y (2004) Orientation relationships of icosahedral quasicrystalline phase and Laves phase precipitates in a ferritic alloy. *Mater Trans* 45:2598–2601. <https://doi.org/10.2320/matertrans.45.2598>
- [23] Versteyley CD, Szymański NK, Sluiter MHF, van Dijk NH (2018) Finite element modelling of creep cavity filling by solute diffusion. *Philos Mag* 98(10):864–877. <https://doi.org/10.1080/14786435.2017.1418097>
- [24] Jang J-W, Kwon J, Lee B-J (2010) Effect of stress on self-diffusion in bcc Fe: an atomistic simulation study. *Scr Mater* 63(1):39–42. <https://doi.org/10.1016/j.scriptamat.2010.02.045>
- [25] Militzer M, Sun WP, Jonas JJ (1994) Modelling the effect of deformation-induced vacancies on segregation and precipitation. *Acta Metall Mater* 42(1):133–141. [https://doi.org/10.1016/0956-7151\(94\)90056-6](https://doi.org/10.1016/0956-7151(94)90056-6)
- [26] Song SH, Chen XM, Weng LQ (2011) Solute diffusion during high-temperature plastic deformation in alloys. *Mater Sci Eng A* 528(24):7196–7199. <https://doi.org/10.1016/j.msea.2011.06.015>
- [27] Shima Y, Ishikawa Y, Nitta H, Yamazaki Y, Mimura K, Isshiki M, Iijima Y (2002) Self-diffusion along dislocations in ultra high purity iron. *Mater Trans* 43(2):173–177. <https://doi.org/10.2320/matertrans.43.173>

Publisher's Note Springer Nature remains neutral with regard to jurisdictional claims in published maps and institutional affiliations.